Melting, freezing, and dynamics of two-dimensional dipole systems in screening bulk media

Ye. K. Aldakul and Zh. A. Moldabekov[*]

Institute of Applied Sciences and IT, 40-48 Shashkin Str., 050038 Almaty, Kazakhstan
and Institute for Experimental and Theoretical Physics, Al-Farabi Kazakh National University, 71 Al-Farabi Str., 050040 Almaty, Kazakhstan

T. S. Ramazanov

Institute for Experimental and Theoretical Physics, Al-Farabi Kazakh National University, 71 Al-Farabi Str., 050040 Almaty, Kazakhstan

This paper reports on the molecular dynamics simulations of classical two-dimensional (2D) electric dipole systems. The properties of 2D systems with bare (nonscreened) and screened dipole-dipole interactions have been investigated. Based on the polygon construction method, we present simulation results on the phase transition, and we locate the melting and freezing points of 2D dipole systems in terms of a polygon disorder parameter, with the polygon disorder parameter being the sum of nontriangular polygon order parameters. It was found that the phase transition of the system occurs when the polygon disorder parameter has a value 0.165. This result was cross-checked by using both local and overall orientational order parameters. We also identified that the value of the average local orientational order parameter at the phase transition point is 0.67. These results are valid for the ordinary (bare) dipole-dipole interaction as well as the screened dipole-dipole interaction, and they are expected to be general for other 2D systems with repulsive pair interaction. We observed that both melting and freezing points shift to lower values of temperature due to screening. In the liquid state, the radial distribution function and polygon construction method show the loss of order in a structure as screening becomes more severe. Furthermore, the impact of screening on the system's collective excitation spectra and diffusive characteristics at liquid and solid states has been studied. Results show the decrease in the values of both longitudinal and transverse sound speeds and the emergence of anomalous superdiffusive motion in the liquid state due to screening.

I. INTRODUCTION

Classical and quantum two-dimensional (2D) systems represent practical as well as fundamental interest [1,2]. The interaction between particles in such systems significantly varies depending on the type of particles, external fields, and other system parameters [1]. We focus on the 2D system of classical particles interacting via a repulsive dipole-dipole potential. The pair dipole-dipole interaction is realized in complex plasmas [3,4] and in a classical 2D monolayer of colloidal systems [5–7]. Polar molecules with a large mean interparticle distance is another example of a system of dipoles [1,8]. Additionally, bound electron-hole excitons in semiconductors create a dipolelike excitonic phase state that can be modeled as a classical 2D system of dipoles [9,10]. The formation of such a phase in electron-hole bilayers was studied by both quantum path integral Monte Carlo simulations [11–13] and classical molecular dynamics simulations [14]. As Tiene *et al.* [15] have recently discussed, screening due to excess charges modifies electron-hole systems, including electron-hole excitons.

Pair interaction potentials can be conditionally classified into long-range and short-range. From a computational point of view, the potential can be considered to be long-ranged if the introduction of the cutoff distance for a pair interaction potential does not allow reducing the scaling of the force computation time to $O(N)$ (e.g., using neighbor lists or cell lists), where the cutoff distance is the distance at which the pair interaction potential is gauged to be negligible for the simulation of a system, and N is the number of particles. Such a potential is often also referred to as a quasi-long-range potential.

As is well known, the presence of charged particles leads to the screening of electrostatic interactions. Screening can result in drastic changes of system properties compared to the case of bare interactions due to the transformation of the long-range pair interaction to the short-range pair interaction [16,17]. A prominent example is given by the comparison of the Coulomb system properties to that of a many-particle system interacting via the Yukawa (Debye-Hückel) potential. Therefore, it is natural and interesting to inquire whether the inclusion of screening has similar dramatic effects on the properties of dipole systems. To this end, the first objective of our research is to study the effect of screening on the properties of 2D dipole systems. In particular, we consider dipoles with parallel dipole moments embedded into a polarizable (screening) bulk medium. Such screened dipole systems are realized in complex plasmas due to a stationary flux of ions relative to charged dust particles [3,4,18–25], where a

[*]zhandos@physics.kz

negatively charged dust particle together with the deformed ion cloud around the dust particle is considered as a compound particle with nonzero dipole moment, and screening of the field of such a compound particle is due to background ideal electrons [3,4,18–25]. Also, we anticipate that such systems with screened dipole-dipole interaction can be realized in the case of colloidal particles immersed in an electrolyte [26,27].

The 2D system with bare dipole-dipole interaction was extensively studied using molecular dynamics (MD) simulation [2,5,9,10,28–30]. Golden *et al.* [10] revealed that for 2D dipole systems, the dispersion of collective oscillations shows an acoustic mode in the long-wavelength limit, and this mode in the classical system is not different from that of quantum systems. Additionally, they showed that the 2D dipole system does not permit a random phase approximation (RPA) -type approximation, i.e., the effect of interparticle correlations is crucial even in the long-wavelength limit, in contrast to, e.g., nonideal Coulomb systems [9,31]. Khrapak *et al.* [2] studied collective excitation spectra, sound speed, and thermodynamics of 2D dipoles from the weakly coupled gas to the strongly correlated fluid and crystalline states. Recently, Mistryukova *et al.* [32] performed a detailed study of the so-called "q-gap" corresponding to the domain of wave vectors where transverse excitations are absent in liquids. To extend these studies, in this paper we present the extensive and systematic study of dynamical and structural properties of 2D dipole systems in screening bulk media. We consider both fluid and solid phases. Furthermore, to gauge the effect of screening, all results are compared to the case of bare dipole-dipole interactions.

Moreover, we investigated the melting and freezing of 2D dipole systems. For that we used an orientational order parameter [33–37] along with a polygon order parameter [38], the latter of which is obtained from a polygon construction method [38,39]. For 2D dipole systems, the behavior of polygon order parameters in the course of melting and freezing was not studied before. Compared to the orientational order parameter, polygon order parameters bear more detailed as well illustrative information about defects in the system, and thus they can be an effective tool for the identification of phase-transition points. Therefore, the second objective of the research presented in this paper is the polygon construction method based identification of the dynamical criterion of melting and freezing in 2D dipole systems.

The paper is organized as follows: In Sec. II we discuss the screened dipole-dipole potential by making use of a Poisson equation in bulk media and multipole expansion. Simulation details are given in Sec. III. Section IV is devoted to results and discussions of structural properties and the phase transition, and in Sec. V we present results of dynamical properties, namely collective excitation spectra and the mean-squared displacement.

II. THE INTERACTION POTENTIAL

First, we briefly discuss a standard multipole expansion method for the derivation of the dipole-dipole interaction potential. This will help us to convey how to generalize this method to the derivation of the interaction potential between dipoles in screening media.
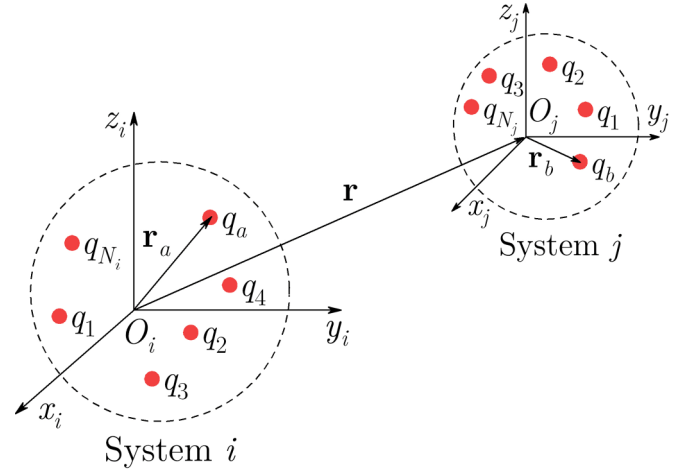

FIG. 1. A supplementary illustration for the discussion of the multipole expansion method for systems with an internal charge distribution.

A. Bare dipole-dipole interaction potential

Consider two systems with a discrete charge distribution as shown in Fig. 1. Denote the first collection of charges as System i and the second one as System j. Let $\mathbf{r}$ be a vector from the origin of System i to the origin of System j, so that $r = |\mathbf{r}|$ is much larger than the characteristic sizes of both systems. Here, our objective is to describe electrostatic interactions between these two systems. As a first step, we examine a potential of System i at a distance r in terms of a multipole expansion. If $\mathbf{r}_a$ is a position vector of charge q_a subject to System i, then the Coulomb potential of this system at $\mathbf{r}$ is given by

$$V(\mathbf{r}) = \frac{1}{4\pi\epsilon_0} \sum_{a=1}^{N_i} \frac{q_a}{|\mathbf{r} - \mathbf{r}_a|}, \qquad (1)$$

where N_i is the number of charges confined in System i. The Taylor expansion of Eq. (1) at $r \gg r_a$ reads

$$V(\mathbf{r}) = \frac{1}{4\pi\epsilon_0} \left(\frac{Q_i}{|\mathbf{r}|} - \mathbf{p}_i \cdot \nabla \frac{1}{|\mathbf{r}|} + \cdots \right), \qquad (2)$$

where $Q_i = \sum_{a=1}^{N_i} q_a$ and $\mathbf{p}_i = \sum_{a=1}^{N_i} q_a \mathbf{r}_a$ are the monopole charge and electric dipole moment of System i, respectively.

Now, one can find the electrostatic potential energy of interaction considering System j is in the electric field created by System i. If $\mathbf{r}_b$ is a position vector of charge q_b subject to System j, then the interaction energy of Systems i and j is given by

$$U = \frac{1}{4\pi\epsilon_0} \sum_{b=1}^{N_j} q_b V(\mathbf{r} + \mathbf{r}_b), \qquad (3)$$

where N_j is the number of charges belonging to System j. The expression for $V(\mathbf{r} + \mathbf{r}_b)$ given in Eq. (2) is further expanded in a Taylor series taking into account that $r \gg r_b$. By substituting the resulting Taylor series into Eq. (3), we have

$$U = \frac{1}{4\pi\epsilon_0} [Q_j V(\mathbf{r}) + \mathbf{p}_j \cdot \nabla V(\mathbf{r}) + \cdots], \qquad (4)$$

where a monopole charge $Q_j = \sum_{b=1}^{N_j} q_b$ and a dipole moment $\mathbf{p}_j = \sum_{b=1}^{N_j} q_b \mathbf{r}_b$ are source charges in System j.

Since we aim to investigate only dipole-dipole interaction, the sum of all moments except the dipole moment in multipole expansions is set to zero. Thus, taking the gradient of the remaining second term in Eq. (2) and substituting the result into Eq. (4), one arrives at the familiar interaction energy of Systems i and j comprised of dipoles,

$$ U = \frac{(\mathbf{p}_i \cdot \mathbf{p}_j)r^2 - 3(\mathbf{p}_i \cdot \mathbf{r})(\mathbf{p}_j \cdot \mathbf{r})}{r^5}. \quad (5) $$

Further, if particles have dipole moments parallel and equal to each other, i.e., $\mathbf{p}_i = \mathbf{p}_j$ and $\mathbf{p}_i \cdot \mathbf{r} = \mathbf{p}_j \cdot \mathbf{r} = 0$, then Eq. (5) reduces to

$$ U = \frac{p^2}{4\pi\epsilon_0 r^3}, \quad (6) $$

where $p = |\mathbf{p}_i| = |\mathbf{p}_j|$, with dipole moments being perpendicular to the monolayer. We refer to potential (6) as the bare dipole-dipole interaction potential.

B. Screened dipole-dipole interaction potential

At large distances, the electric field of System i in the screening bulk media satisfies the following Poisson equation:

$$ \left(\Delta + k_s^2\right)V_s(\mathbf{r}) = -\frac{1}{\epsilon_0}\sum_{a=1}^{N_i} q_a \delta(\mathbf{r} - \mathbf{r}_a), \quad (7) $$

where k_s is the inverse screening length due to polarization of the bulk media, and the subscript s denotes the screened potential. Making use of the Green's function of the equation $(\Delta + k_s^2)G(\mathbf{r}', \mathbf{s}) = \delta(\mathbf{r}' - \mathbf{s})$,

$$ G(\mathbf{r}, \mathbf{s}) = -\frac{1}{4\pi}\frac{\exp(-k_s|\mathbf{r} - \mathbf{s}|)}{|\mathbf{r} - \mathbf{s}|}, $$

it is straightforward to find the following solution of Eq. (7):

$$ V_s(\mathbf{r}) = -\frac{1}{\epsilon_0}\int d\mathbf{s}\, G(\mathbf{r}, \mathbf{s})\left\{\sum_{a=1}^{N_i} q_a \delta(\mathbf{s} - \mathbf{r}_a)\right\} $$
$$ = \frac{1}{4\pi\epsilon_0}\sum_{a=1}^{N_i}\frac{q_a \exp(-k_s|\mathbf{r} - \mathbf{r}_a|)}{|\mathbf{r} - \mathbf{r}_a|}. \quad (8) $$

From the comparison of Eq. (8) with Eq. (1), we understand that to get the screened dipole-dipole interaction potential, one must use the screened potential (8) instead of the Coulomb potential in the multipole expansion given in Sec. II A. The Taylor expansion of Eq. (8) has the same form as Eq. (2), with the difference being that the kernel $1/|\mathbf{r}|$ has to be replaced with $\exp(-k_s|\mathbf{r}|)/|\mathbf{r}|$, i.e.,

$$ V_s(\mathbf{r}) = \frac{1}{4\pi\epsilon_0}\left(\frac{Q_i \exp(-k_s|\mathbf{r}|)}{|\mathbf{r}|}\right.$$
$$ \left. -\mathbf{p}_i \cdot \nabla\frac{\exp(-k_s|\mathbf{r}|)}{|\mathbf{r}|} + \cdots\right). \quad (9) $$

The potential energy is obtained by placing $V_s(\mathbf{r} + \mathbf{r}_b)$ instead of $V(\mathbf{r} + \mathbf{r}_b)$ in Eq. (3). Then, once again taking the Taylor expansion of $V_s(\mathbf{r} + \mathbf{r}_b)$ at $r \gg r_b$, one derives

$$ U = \frac{1}{4\pi\epsilon_0}[Q_j V_s(\mathbf{r}) + \mathbf{p}_j \cdot \nabla V_s(\mathbf{r}) + \cdots]. \quad (10) $$

Equations (9) and (10) enable us to describe any system comprised of screened point charges, dipoles, quadrupoles, etc. As we are interested in systems consisting only of electric dipoles, setting $Q_i = Q_j = 0$ and neglecting quadruple and higher-order terms in Eq. (10), we get the appropriate equation for the screened electrostatic interaction energy of dipoles:

$$ U = \frac{\exp(-k_s r)}{4\pi\epsilon_0 r^5}\{[(\mathbf{p}_i \cdot \mathbf{p}_j)r^2 - (\mathbf{p}_i \cdot \mathbf{r})(\mathbf{p}_j \cdot \mathbf{r})(3 + k_s r)] $$
$$ \times (1 + k_s r) + (\mathbf{p}_i \cdot \mathbf{r})(\mathbf{p}_j \cdot \mathbf{r})k_s r\}. \quad (11) $$

Since we consider the case when compound particles have dipole moments parallel and equal to each other, Eq. (11) reduces to

$$ U = \frac{p^2 \exp(-k_s r)}{4\pi\epsilon_0 r^3}(1 + k_s r). \quad (12) $$

The associated interaction force is given by

$$ \mathbf{F}_{ij} = -\boldsymbol{\nabla}U = \frac{p^2 \exp(-k_s r)}{4\pi\epsilon_0 r^4}\left(3 + 3k_s r + k_s^2 r^2\right)\hat{\mathbf{r}}_{ij}, $$

where the subscript ij indicates the force exerted by dipole i on dipole j, and $\hat{\mathbf{r}}_{ij} = \mathbf{r}/r$ is a unit vector directed from i to j.

III. SIMULATION DETAILS

We considered the ensemble of point particles with the pair interaction potential given by Eq. (6) or (12). MD simulations of the system consisting of $N = 5041$ identical particles confined in a 2D square box have been performed. A side length of the box is determined by the number of particles, i.e., $L = \sqrt{\pi N}a$, where a is the mean interparticle distance, which is directly related to the areal density of particles n through the equation $a = (\pi n)^{-1/2}$. In a crystalline structure, a refers to the Wigner-Seitz radius. To discard the boundary effects, periodic boundary conditions were used. The convenient choices of basic units are a for the units of length, the inverse characteristic dipole oscillation frequency $\omega_D^{-1} = [p^2/(2\pi\epsilon_0 ma^5)]^{-1/2}$ for the units of time, and $\varepsilon = p^2/(4\pi\epsilon_0 a^3)$ for the units of energy. There are two dimensionless parameters that set up the conditions of the model system. First, the coupling parameter $\Gamma_D = p^2/(4\pi\epsilon_0 a^3 k_B T)$, which is defined as the ratio of the potential energy at a distance a to the thermal kinetic energy of particles. Second, the screening parameter $\kappa = ak_s$, i.e., the reduced inverse screening length.

We focused on the investigation of the liquid and solid states of dipoles and the impact of screening on such systems. For these states, the value of the coupling parameter is set to $\Gamma_D = 60$ and 500 corresponding to liquid and solid phases, respectively. The agreement of the prescribed coupling parameter values to the stated phases is shown in Sec. IV A. For a given value of the coupling parameter, we varied the screening parameter as $\kappa = 0$, 1, and 2. The results of the following

sections, devoted to structural and dynamical properties, were measured and averaged over $1000\omega_D^{-1}$ periods of time.

In the case of the bare dipole-dipole interaction potential (6), i.e., $\kappa = 0$, a direct summation of the interaction force is highly time-consuming. To maintain the accuracy of the calculations, one needs to generate a rather large number of particles. The quasi-long-range character of the bare potential can be circumvented by many methods [40–43]. To avoid a direct summation scaling as $O(N^2)$, we used gradient-shifted force (GSF) electrostatics [44] based on the Wolf method [45], which scales as $O(N)$. In GSF electrostatics, the damping coefficient α and the cutoff radius r_c should be assigned appropriate values. For a commonly used cutoff value $r_c = 12\,a$, the optimal value of the damping coefficient was shown to lie in the range $0.175 \leqslant \alpha\,a \leqslant 0.225$ [46]. Hence, in our simulations we set $r_c = 12\,a$ and $\alpha = 0.2\,a^{-1}$.

IV. STRUCTURAL PROPERTIES AND PHASE TRANSITION

A. Structural properties in liquid and solid states

To see the overall features of the system structure and the changes due to the screening effect, we calculated the radial distribution function (RDF), which shows the dependence of the particles' density distribution on a radial distance from any reference particle. The results of the RDF calculations are shown in Fig. 2. At all the considered values of κ, from Fig. 2 one can see that $\Gamma_D = 60$ and 500 corresponds to liquid and solid phases, respectively. At $\Gamma_D = 60$, and for all three values of κ in Fig. 2(a), the monotonically decreasing maxima and increasing minima of curves with distance r definitely indicate a liquidlike structure. In the same manner, at $\Gamma_D = 500$, the curves in Fig. 2(b) with their sharp first maximum and zero first minimum ($R \neq 0$), followed by the irregularly spaced maxima and minima, describe the solid state, again for all three values of κ. Note that for $\Gamma_D = 60$ and $\kappa = 0$, our data on RDF are in agreement with the results of Ref. [9].

Further analysis of the curves shows that in both liquid and solid states, the screening effect leads to a decrease of order in the system. To be more specific, at $\Gamma_D = 60$ the first maximum of RDF drops from about $g_{\max}^{\kappa=0} \approx 2.85$ (where a subscript refers to the maximum or minimum and a superscript denotes the value of κ) to $g_{\max}^{\kappa=1} \approx 2.66$ and then to $g_{\max}^{\kappa=2} \approx 2.16$, and the corresponding first minimum ($R \neq 0$) increases as $g_{\min}^{\kappa=0} \approx 0.34$, $g_{\min}^{\kappa=1} \approx 0.42$, and $g_{\min}^{\kappa=2} \approx 0.58$. Performing the same analysis of data at $\Gamma_D = 500$, we find for nonscreened dipoles $g_{\max}^{\kappa=0} \approx 8.87$ and for successive screening values $g_{\max}^{\kappa=1} \approx 8.19$ and $g_{\max}^{\kappa=2} \approx 5.98$. As can be seen from Fig. 2(b), the first minimum ($R \neq 0$) in this case stays nearly at zero, $g_{\min}^{\kappa=0} \approx g_{\min}^{\kappa=1} \approx g_{\min}^{\kappa=2} \approx 0$.

The RDF gives a very nice qualitative and quantitative description of the structure as long as the state of the system under investigation does not change over time. Otherwise, the lack of ensemble averaging gives poor RDF results, especially in the case of MD simulations. It is clear that the RDF may not be suitable for the analysis of structural changes if the system is heated or cooled. For this reason, and also for a better description of the structural properties, we use two additional tools, namely an orientational order parameter (OOP)
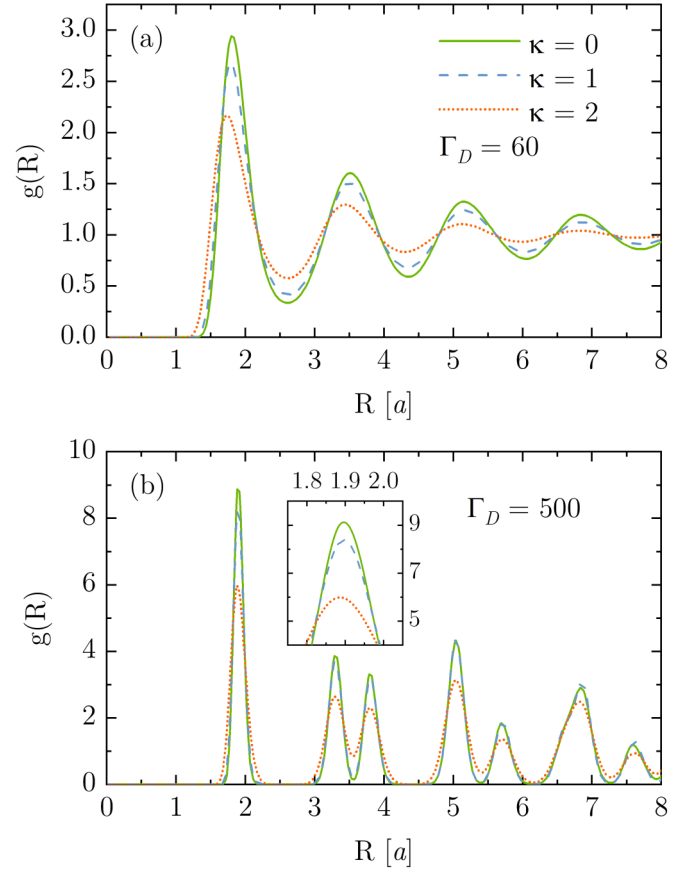

FIG. 2. The radial distribution function (RDF) of dipole particles at (a) liquid ($\Gamma_D = 60$) and (b) solid ($\Gamma_D = 500$) states for three values of screening parameter κ.

[33–37] and a polygon construction method [38,39]. For the investigation of the phase transition, these are major tools of analysis and for indicating phase transitions points. By studying the behavior of different order parameters during melting and freezing, we have drawn important general conclusions as discussed below.

The OOP was introduced by Halperin and Nelson in their work on the 2D melting [33,34]. For a triangular lattice structure, the OOP for particle j is defined as

$$\psi_j = \frac{1}{N_j} \sum_{k=1}^{N_j} \exp\left(6i\theta_{jk}\right), \tag{13}$$

where N_j is the number of nearest-neighbor particles, i is the imaginary unit, and θ_{jk} is the angle between an arbitrary fixed direction, in our case the x-axis, and a bond connecting particles j and k. Due to the fact that parameter ψ_j is complex-valued, it can be measured in two ways. The first way defines the overall orientational order of the system, and it has the form [36,47]

$$|\langle\psi\rangle| = \left|\frac{1}{N} \sum_{j=1}^{N} \psi_j\right|, \tag{14}$$

that is, one takes the average over all particles and then measures the absolute value. The second way is to first take the

TABLE I. The reduced potential energy per particle, overall and local orientational, and polygon order parameters of the 2D electric dipole system at the liquid state, $\Gamma_D = 60$, and the respective values of κ.

κ	$\overline{\langle U \rangle}/\varepsilon$	$\overline{|\langle \psi \rangle|}$	$\overline{\langle |\psi| \rangle}$	$\overline{P_3}$	$\overline{P_4}$	$\overline{P_5}$	$\overline{P_6}$
0	0.593	0.06 ± 0.03	0.593 ± 0.006	0.517 ± 0.007	0.180 ± 0.004	0.029 ± 0.002	0.0015 ± 0.0004
1	0.231	0.03 ± 0.02	0.553 ± 0.004	0.452 ± 0.006	0.188 ± 0.003	0.041 ± 0.002	0.0037 ± 0.0006
2	0.065	0.015 ± 0.008	0.503 ± 0.004	0.338 ± 0.005	0.181 ± 0.003	0.064 ± 0.002	0.015 ± 0.001

absolute value and then calculate the average [48,49], i.e.,

$$\langle |\psi| \rangle = \frac{1}{N} \sum_{j=1}^{N} |\psi_j|. \quad (15)$$

The last one gives information about the average local orientational order of the whole system. In perfect defect-free structure, the value of both $|\langle \psi \rangle|$ and $\langle |\psi| \rangle$ is close to unity and drops as the disorder spreads over the system.

The other tool for analyzing the structural properties of the system is the polygon construction method of Glaser and Clark [38,39]. This method describes defects in the system by identifying an excess volume in the arrangement of particles. In the polygon construction method, one starts by measuring the position of each particle. Then, using a Delaunay triangulation, bonds are created between neighboring particles. To identify defects in the structure, some of the bonds are removed. A bond subject to removal is identified in two ways: either the bond is too long or the angle opposite to that bond is too large. Thus, one can choose between the bond-length or bond-angle approach for identifying long bonds for removal. In the bond-length approach, a bond is considered to be long if it exceeds the threshold bond length l_{th}. The threshold bond length should have a value in the range $b < l_{\text{th}} < \sqrt{2}b$, where b corresponds to a lattice constant of the given structure [38,39]. In the same manner, in the bond-angle approach a bond is removed if the opposite angle to the bond exceeds the value of threshold angle θ_{th}, where θ_{th} is assigned a value in the range $60° < \theta_{\text{th}} < 90°$ [38,39]. In this work, we use the latter approach and set $\theta_{\text{th}} = 75°$.

The result of the polygon construction method is a map of polygons consisting of triangles, quadrilaterals, pentagons, etc. The perfect defect-free structure consists only of triangles, and the presence of any nontriangular polygons indicates defects in the system. Hence in the polygon construction method, polygons with more than three sides are defined as geometrical defects [38,39]. Nontriangular polygons do not emerge chaotically with the increase of imperfections in the structure. Instead, as the disorder progresses, the abundance of nontriangular polygons follows a pattern, with quadrilaterals being the most abundant, followed by pentagons, then

hexagons, etc. Therefore, by examining the quantity of each geometrical defect, one can have a better insight into the severity of disorder. Quadrilaterals can be viewed as the least severe defects, while pentagons, hexagons, etc. are progressively more severe [50].

In addition to providing visual information, the polygon construction method defines a quantity called the polygon order parameter [38]. This parameter provides information about the fraction of a certain polygon type in the system, and it is calculated by the equation

$$P_p = \frac{N_p}{2N}, \quad (16)$$

where N_p is the number of polygons with p ($p = 3, 4, 5, 6$) sides. From a geometric perspective, P_3 can be understood as an "order" parameter while the sum of $P_4 + P_5 + P_6$ we refer to as the disorder parameter.

That being said, we have calculated the above-discussed order parameters along with the values of reduced potential energy per particle and changes in these quantities due to the screening effect. Results are presented in Tables I and II, where a bar over the quantities indicates the time averaging, and the uncertainty of the mean value of order parameters corresponds to one standard deviation (i.e., 68.27% confidence interval). First of all, we see that at both $\Gamma_D = 60$ and 500 the effect of screening is reflected by a drop in potential energy of about 60% when the screening parameter is changed from $\kappa = 0$ to 1, and a drop in energy of about 90% at $\kappa = 2$ compared to the case $\kappa = 0$. This, in turn, implies the emergence of disorder in the system structure, which is also indicated by the changes in order parameters. To be more precise, the order parameters $\overline{|\langle \psi \rangle|}$, $\overline{\langle |\psi| \rangle}$, and $\overline{P_3}$ undergo a decline while the disorder parameter $\overline{P_4} + \overline{P_5} + \overline{P_6}$ proliferate as we change the screening parameter from $\kappa = 0$ to 1 and then to $\kappa = 2$.

Next, in addition to RDF results shown in Fig. 2, the fact that $\Gamma_D = 60$ corresponds to the liquid and $\Gamma_D = 500$ to the solid state can be confirmed by noting the values of $\overline{|\langle \psi \rangle|}$ and $\overline{\langle |\psi| \rangle}$. In Table I we notice $\overline{|\langle \psi \rangle|} < 0.1$ and $\overline{\langle |\psi| \rangle} < 0.6$, which indicates that the system has no rigid structure, but it has that of liquid. And in Table II, OOPs have values close to unity, which corresponds to a solid structure.

TABLE II. The reduced potential energy per particle, overall and local orientational, and polygon order parameters of the 2D electric dipole system at the solid state, $\Gamma_D = 500$, and the respective values of κ.

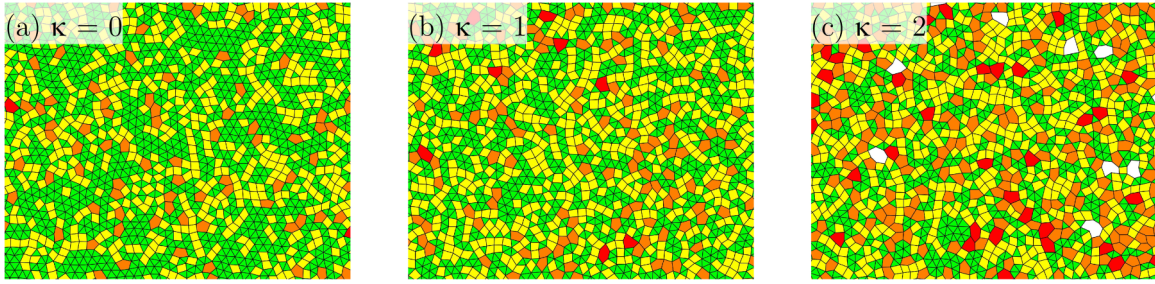| κ	$\overline{\langle U \rangle}/\varepsilon$	$\overline{|\langle \psi \rangle|}$	$\overline{\langle |\psi| \rangle}$	$\overline{P_3}$	$\overline{P_4}$	$\overline{P_5}$	$\overline{P_6}$
0	0.5729	0.9591 ± 0.0005	0.9680 ± 0.0004	0.9701 ± 0.0003	0.0006 ± 0.0002	0.00006 ± 0.00006	0
1	0.2114	0.9512 ± 0.0008	0.9621 ± 0.0006	0.9701 ± 0.0004	0.0008 ± 0.0002	0.00004 ± 0.00003	0
2	0.0495	0.905 ± 0.002	0.925 ± 0.001	0.957 ± 0.002	0.0070 ± 0.0008	0.00010 ± 0.0008	0

FIG. 3. An illustration of the polygon construction method applied to the 2D dipole system structure at $\Gamma_D = 60$ and the successive values of κ. Sample figures correspond to the calculations given in Table I. Here, the triangles are shown in green, quadrilaterals in yellow, pentagons in orange, hexagons in red, and the polygons with seven or more sides are in white.

Figure 3 illustrates the use of the polygon construction method, which corresponds to calculations presented in Table I. In Fig. 3, vertices match the positions of particles and all alike polygons drawn with the same color: triangles, green; quadrilaterals, yellow; pentagons, orange; hexagons, red; and polygons with seven or more sides, white. We are able to observe visually the liquid structure and the emergence of more abundant geometrical defects as a result of the stronger screening.

B. Melting and freezing of 2D dipole systems

In this section, we explore the solid-liquid phase transition of 2D electric dipole systems, and we investigate the influence of screening on a solid-liquid phase transition point. The setup of the model system is the same as before, with the difference being that now the temperature of the system is controlled by a thermostat. The simulations of a phase transition are comprised of two stages. In the first stage, we start from a crystal phase by setting the initial value of the coupling parameter to $\Gamma_D = 500$, which corresponds to a temperature value of $T = 0.002\,\varepsilon/k_B$. Initially, the system is thermalized over the $5000\,\omega_D^{-1}$ periods of time to ensure that an equilibrium state is prepared. After that, the system is heated with a constant rate equal to $dT/dt = 10^{-6}\,\varepsilon\omega_D/k_B$ until the final value of the coupling parameter $\Gamma_D = 50$, i.e., temperature $T = 0.02\,\varepsilon/k_B$, is achieved. By noting that the initial and final values of the coupling parameter should correspond to solid and liquid states, respectively, we expect to capture a solid to liquid phase transition (melting) point during the heating period. In the second stage of simulation, the system starts at $\Gamma_D = 50$. Here, the system is gradually cooled at the same rate

$dT/dt = 10^{-6}\,\varepsilon\omega_D/k_B$ until $\Gamma_D = 500$ is reached again. By doing so, we are able to obtain a liquid to solid phase transition (freezing) point. We note that if the rate of temperature change is too fast, the system loses its equilibrium state and becomes erratic far beyond the proper phase transition points. The chosen rate $dT/dt = 10^{-6}\,\varepsilon\omega_D/k_B$ was found to be optimal in terms of the computational effort and the quality of the results, and the slower rates must not affect the results substantially. To dampen the fluctuations in the measured quantities during phase transition simulations, the averaging has been done over five simulation runs.

Melting and freezing points can be identified by inspecting the values of the potential energy, and the orientational and polygon order parameters. In Figs. 4–6, plots of these quantities versus temperature are presented, where arrows serve to discern two stages of the simulation. The abrupt change in the values of measured quantities during heating and cooling periods is the sign of the phase transition.

If we first consider the nonscreened case, when the screening parameter $\kappa = 0$, we notice the potential energy in Fig. 4(a), and the disorder parameter in Fig. 6 undergoes a sudden increase while overall [Fig. 5(a)] and local [Fig. 5(b)] OOPs drop to values $|\langle\psi\rangle| < 0.1$ and $\langle|\psi|\rangle < 0.6$. These changes are a signature of melting, and we find that melting takes place in the temperature interval $0.0150 < k_B T_m^{\kappa=0}/\varepsilon < 0.0162$ (where a subscript indicates melting). Then, as the system is gradually cooled, an abrupt drop in the potential energy and the disorder parameter and an increase of OOPs is observed, which we understand to be freezing of the system. We find that freezing occurs in the interval $0.0131 < k_B T_f^{\kappa=0}/\varepsilon < 0.0145$ (where a subscript indicates freezing).
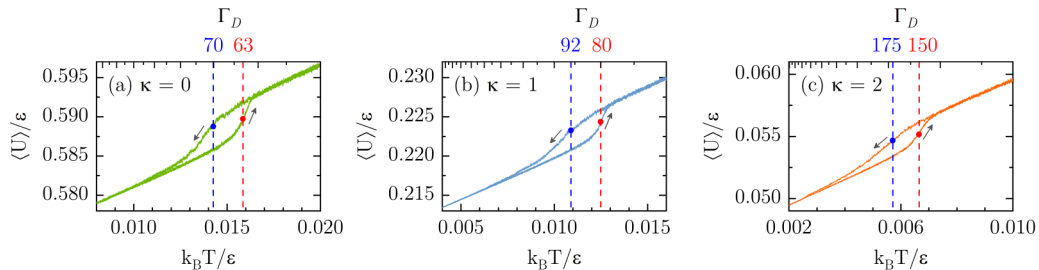

FIG. 4. The potential energy profile of 2D electric dipole systems during the heating and cooling periods: (a) at no screening, (b) at $\kappa = 1$, and (c) at $\kappa = 2$. Red (light gray) and blue (dark gray) vertical dashed lines pass through the melting and freezing points, respectively, and indicate the coupling parameter values at which phase transition occurs.
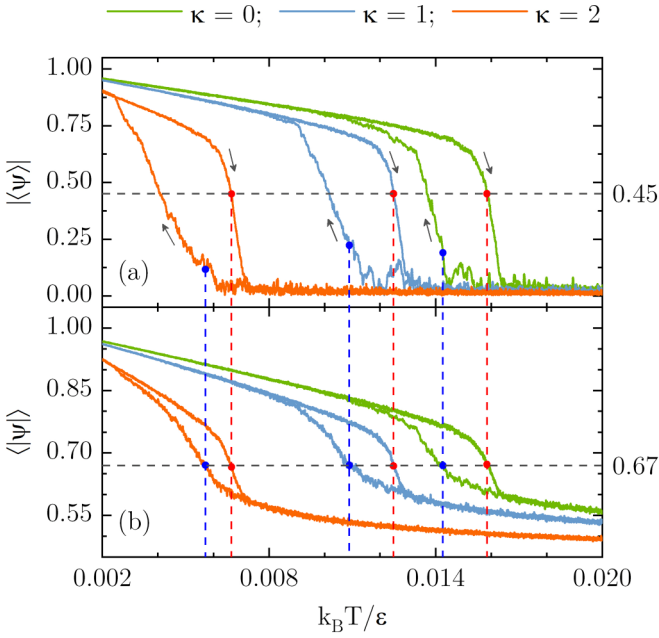
FIG. 5. The overall (a) and local (b) orientational order parameters (OOPs) measured during the heating and cooling periods. Red (light gray) and blue (dark gray) dots are the melting and freezing points with red (light gray) and blue (dark gray) vertical dashed lines passing through these points. The green (rightmost), blue (mid), and orange (leftmost) curves correspond to $\kappa = 0$, 1, and 2, respectively.

Next we set $\kappa = 1$. By examining the data in Figs. 4(b), 5, and 6, we obtain the melting range to be $0.0121 < k_B T_m^{\kappa=1}/\varepsilon < 0.0128$ and the range of freezing $0.0092 < k_B T_f^{\kappa=1}/\varepsilon < 0.0109$. The same analysis of curves at $\kappa = 2$ reveals the interval of melting $0.0063 < k_B T_m^{\kappa=2}/\varepsilon < 0.0069$ and the freezing interval $0.0046 < k_B T_f^{\kappa=2}/\varepsilon < 0.0062$.

Two things are obvious from the above-presented results. First, we see that melting and freezing do not follow the same path.
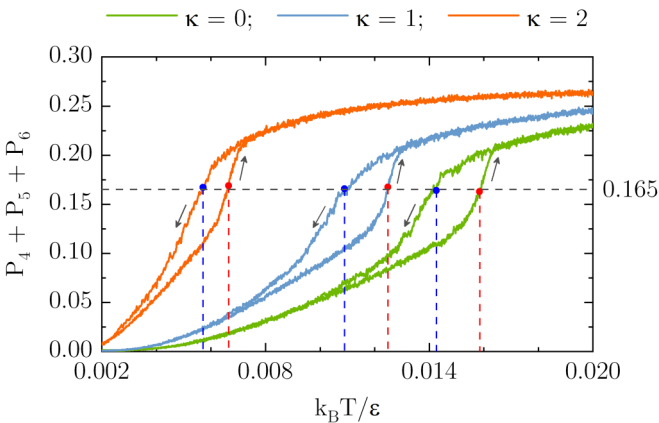

FIG. 6. The disorder parameter obtained from the polygon construction method shows the quantitative measure of disorder during the heating and cooling periods. Red (light gray) and blue (dark gray) vertical dashed lines pass through melting and freezing points and cross the curves when the disorder parameter approximately equals 0.165. The green (rightmost), blue (mid), and orange (leftmost) curves correspond to $\kappa = 0$, 1, and 2, respectively.

path. This is revealed by the emergence of hysteresis in all quantities. The hysteresis was also observed in the study of classical Coulomb systems, where it was shown that hysteresis results due to finite melting and cooling rates, and no hysteresis occurs in the case of infinite simulation time (i.e., an infinitesimally small heating/cooling rate) [37,49]. Here, we extend this statement to electric dipole systems, and we explain the cause of hysteresis by the finite rate of temperature change.

Second, the shifts of phase transition points to lower values of temperature are observed as κ increases. Also, it is worth noting that data presented in Figs. 4–6 show a correlation in measured quantities. For example, during the heating period at the point where the potential energy starts to show signs of melting, the orientational order and disorder parameters also capture this point, reflected by the abrupt increase of the downward and upward trend of the curves, respectively. The same is true when the system is cooled and undergoes freezing.

From the inspection of data in Figs. 4–6 we found only intervals of melting and freezing, and we have not yet addressed the exact phase transition points. It is clear that melting and freezing points of the system should occur somewhere in the above-estimated ranges, but to find where exactly we refer to the universality feature of the overall OOP [37]. Schweigert *et al.* [37] have formulated that melting of 2D lattices occurs when the overall OOP becomes $|\langle \psi \rangle| \approx 0.45$, at which point the overall OOP drops abruptly to values close to zero due to the loss of order in the system [e.g., such behavior can be seen in Fig. 5(a)]. The authors ran simulations with bare and screened Coulomb, Lennard-Jones, and $1/r^{12}$ repulsive interaction potentials, and they checked the validity of the criteria for these systems. Positive results allowed them to conclude about the universality of the proposed criterion [37].

Thus, in order to find exact melting points, we look for those points in Fig. 5(a) where curves cross $|\langle \psi \rangle| \approx 0.45$, which is drawn as the horizontal black dashed line. By locating intersection points and drawing projection lines, which are red vertical dashed lines, to the temperature axis, we obtain melting points for successive screening parameters as $T_m^{\kappa=0} \approx 0.0159\,\varepsilon/k_B$, $T_m^{\kappa=1} \approx 0.0125\,\varepsilon/k_B$, and $T_m^{\kappa=2} \approx 0.0067\,\varepsilon/k_B$. Also, if we look from the viewpoint of $\langle |\psi| \rangle$ shown in Fig. 5(b), we notice that melting of the system occurs when the local OOP attains the value $\langle |\psi| \rangle \approx 0.67$. The conclusion is drawn from the observation that the value 0.67 corresponds to the intersection of $\langle |\psi| \rangle$ curves with the red dashed projection lines of melting points. To locate exact freezing points during the cooling period, we perform the same analysis. But now, liquid to solid transitions are found from Fig. 5(b) by locating points where curves cross 0.67. The freezing points found in this way are $T_f^{\kappa=0} \approx 0.0143\,\varepsilon/k_B$, $T_f^{\kappa=1} \approx 0.0109\,\varepsilon/k_B$, and $T_f^{\kappa=2} \approx 0.0057\,\varepsilon/k_B$.

In Fig. 5, melting points are correctly spotted by both overall and local OOP, but when it comes to freezing points there is inconsistency between $|\langle \psi \rangle|$ and $\langle |\psi| \rangle$ indicated by blue vertical dashed lines passing though the freezing points. The values of $|\langle \psi \rangle|$ are well below the reference value 0.45, whereas $\langle |\psi| \rangle$ marks freezing of the system. The reason behind the low values of $|\langle \psi \rangle|$ lies in the fact that it detects domains in the structure with different overall orientational order [48,49],
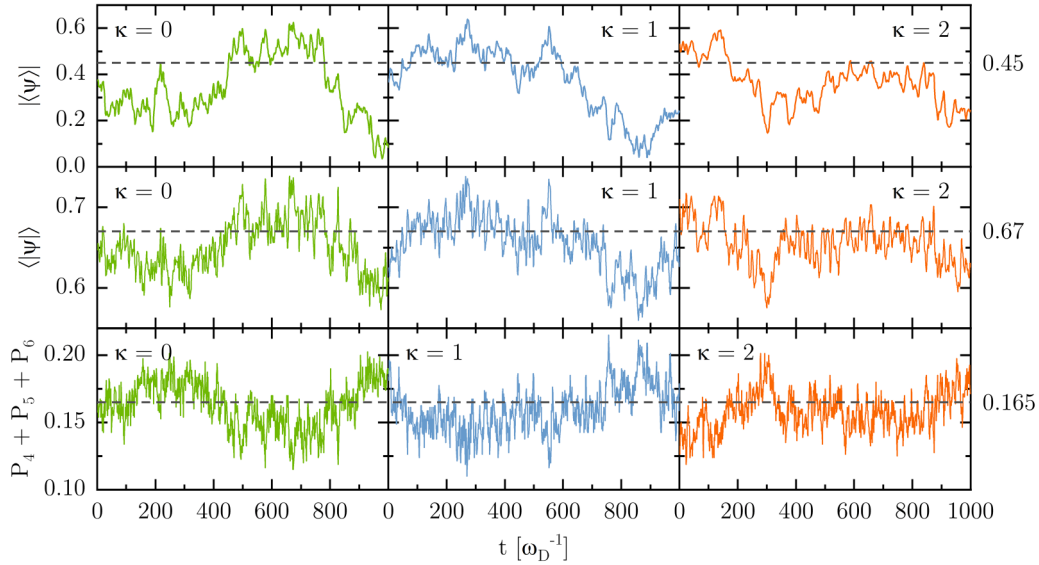
FIG. 7. The evolution of orientational order parameters (OOPs) and disorder parameter at the fixed values of temperature (close to the phase transition point). The prescribed temperatures are $T^{\kappa=0} = 0.01488 \, \varepsilon/k_B$, $T^{\kappa=1} = 0.01157 \, \varepsilon/k_B$, and $T^{\kappa=2} = 0.00594 \, \varepsilon/k_B$ for three cases of screening.

and ψ_j of these different domains tends to cancel each other when $|\langle\psi\rangle|$ is computed using Eq. (14). The initial state of the system during the cooling period corresponds to liquid, and as cooling gradually progresses, metastable domains are formed giving rise to the above-mentioned inconsistency. It is important to note that such a process was observed in the experiment on freezing of colloidal monolayers composed of diameter-tunable microgel spheres [48]. Therefore, the observed inconsistency in detecting the freezing point between $|\langle\psi\rangle|$ and $\langle|\psi|\rangle$ is not merely a simulation artifact. For this reason, we come to the conclusion that liquid to solid phase transition points should be found relying on the local OOP, i.e., one should use Eq. (15) rather than Eq. (14). Note that in the heating period of phase transition simulations, the system starts from an equilibrium structure (perfect crystal) that is free of domains with different orientational order, and as a result $|\langle\psi\rangle|$ correctly detects solid to liquid phase transition points.

The conclusions reached on melting and freezing points by analyzing OOPs were used to analyze the behavior of the disorder parameter during melting and freezing as presented in Fig. 6. The red and blue vertical dashed lines indicate melting and freezing points, respectively, and they cross the curves of the disorder parameter when they are approximately equal to 0.165 (shown as a black horizontal dashed line). Hence, according to the disorder parameter, the phase transition of the system occurs when the sum of nontriangular polygon order parameters, in other words $P_4 + P_5 + P_6$ [see Eq. (16)], reaches a value of 0.165. Since the disorder parameter is based on the geometrical description of the structure, it may as well serve as another universal parameter for identifying phase transition points.

Turning our attention to Fig. 4 once again, we find for three cases of screening that melting of the system occurs when the potential energy per particle becomes $\langle U\rangle_m^{\kappa=0} \approx 0.5897 \, \varepsilon$, $\langle U\rangle_m^{\kappa=1} \approx 0.2244 \, \varepsilon$, and $\langle U\rangle_m^{\kappa=2} \approx 0.0552 \, \varepsilon$. And freezing

occurs when $\langle U\rangle_f^{\kappa=0} \approx 0.5887 \, \varepsilon$, $\langle U\rangle_f^{\kappa=1} \approx 0.2233 \, \varepsilon$, and $\langle U\rangle_f^{\kappa=2} \approx 0.0547 \, \varepsilon$.

It should be noted, however, that the obtained melting and freezing points and respective potential energy values are for a finite rate of temperature change. Thus, based on the above-presented results, we report that the true phase transition points of 2D electric dipole systems with bare and screened interactions must lie in the intervals $\Gamma_D^{\kappa=0} = 67 \pm 4$, $\Gamma_D^{\kappa=1} = 86 \pm 6$, and $\Gamma_D^{\kappa=2} = 163 \pm 13$.

In Refs. [37,49], by performing equilibrium MD simulation at different values of temperature, it was shown that over the course of the phase transition there is an interval of temperatures around the phase transition point within which Coulomb systems have the same probability to exist in crystalline and liquid states. We observed similar behavior in the case of 2D dipole systems. This is illustrated in Fig. 7, where the evolution of OOPs and the disorder parameter is shown as a function of time for three cases of screening at temperature values $T^{\kappa=0} = 0.01488 \, \varepsilon/k_B$, $T^{\kappa=1} = 0.01157 \, \varepsilon/k_B$, and $T^{\kappa=2} = 0.00594 \, \varepsilon/k_B$. Here the thermostat was switched on during simulations to keep the temperature at the prescribed value. From Fig. 7 we see that the system switches between crystalline and liquid states. Therefore, the effect of hysteresis is most likely due to the finite heating and cooling rates. In other words, we conclude that there should be no distinct hysteresis in the limit of infinitesimally small rates of heating and cooling.

V. THE EFFECT OF SCREENING ON DYNAMICAL PROPERTIES

A. Longitudinal and transverse waves

The dynamical properties of bare and screened 2D electric dipole systems have been examined during the calculation of the longitudinal and transverse collective dispersion modes and the mean-square displacement of particles. Longitudinal
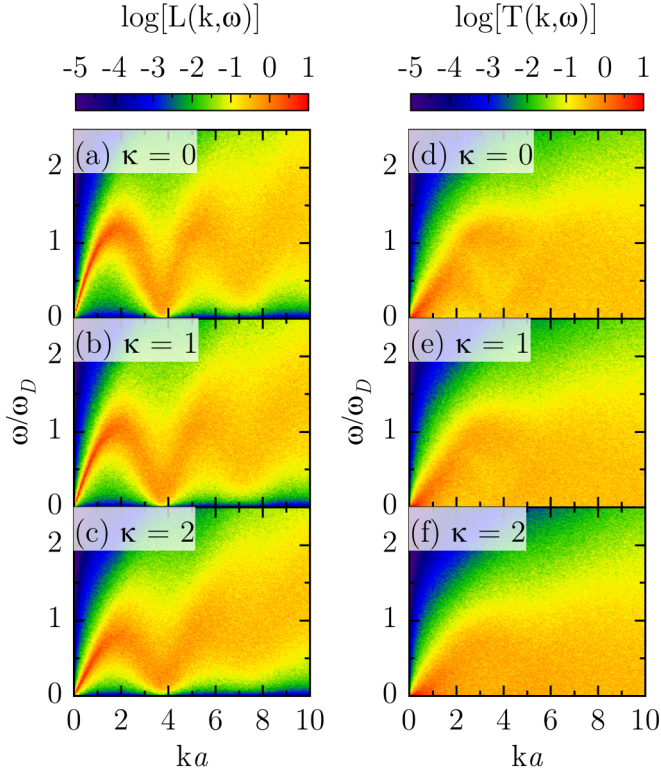
FIG. 8. (a)–(c) Longitudinal and (d)–(f) transverse dispersion relations of 2D electric dipole systems. Results correspond to the liquid state ($\Gamma_D = 60$) and the different strengths of the screening controlled by κ.
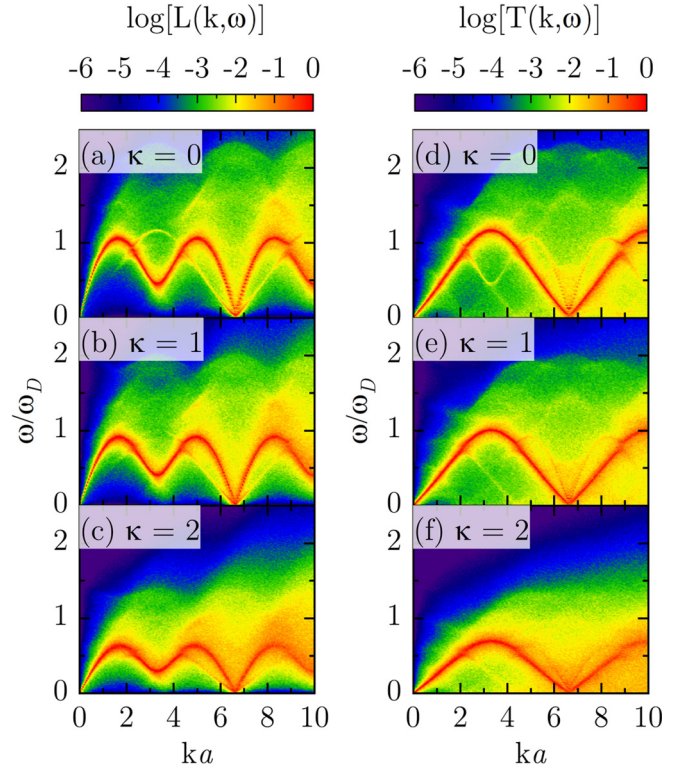

FIG. 9. (a)–(c) Longitudinal and (d)–(f) transverse dispersion relations of 2D electric dipole systems. Results correspond to the solid state ($\Gamma_D = 500$) and the different strengths of the screening controlled by κ.

and transverse collective excitation spectra were computed using the following equations [51]:

$$L(k, \omega) = \frac{1}{2\pi N t_{\mathrm{meas}}} |\mathscr{F}_t[\lambda(k, t)]|^2,$$

$$T(k, \omega) = \frac{1}{2\pi N t_{\mathrm{meas}}} |\mathscr{F}_t[\tau(k, t)]|^2,$$

where t_{meas} stands for the measurement time, $\mathscr{F}_t$ denotes the temporal Fourier transform, and $\lambda(k, t)$ and $\tau(k, t)$ are the longitudinal and transverse components of the microscopic current $\mathbf{j}(\mathbf{k}, t) = \sum_{j=1}^{N} \mathbf{v}_j(t) \exp(i\mathbf{k} \cdot \mathbf{r}_j(t))$, which are given by

$$\lambda(k, t) = \sum_{j=1}^{N} v_{jx}(t) \exp(ikx_j(t)), \tag{17}$$

$$\tau(k, t) = \sum_{j=1}^{N} v_{jy}(t) \exp(ikx_j(t)). \tag{18}$$

In Eqs. (17) and (18), the components of velocity $\mathbf{v}_j(t)$ and position $\mathbf{r}_j(t)$ vectors of particle j at time t are obtained by the MD simulation, and k is the wave number corresponding to the wave vector taken to be parallel to the x-axis.

We calculated microscopic currents given by Eqs. (17) and (18), and then we performed the temporal Fourier transform to obtain the data of the longitudinal $L(k, \omega)$ and transverse $T(k, \omega)$ current fluctuation spectra. To smooth out the data

and obtain the most reliable results, the calculations have been averaged over 10 simulation runs, where in each run $t_{\mathrm{meas}} = 1000 \, \omega_D^{-1}$. The results of the corresponding dispersion relations (i.e., the dependence of the collective oscillation wave frequency ω on the wave number k) are shown in Figs. 8 and 9. The dispersion shown in Fig. 8 describes the liquid state at the value of the coupling parameter $\Gamma_D = 60$ and different values of the screening parameter κ. Note that for $\kappa = 0$ and $\Gamma_D = 60$, our data are in agreement with the results of Ref. [9]. In Fig. 8, we observe an increase of the peak width with an increase in wave number, which implies a shorter lifetime of excitations at larger wave numbers. Both longitudinal and transverse excitation spectra become more degraded as κ increases. The tendency of peaks to spread with respect to κ is also seen in Fig. 9, which corresponds to the solid state with $\Gamma_D = 500$. However, in this case peaks are narrower and have a typical pattern for solid systems with the feature of preserving long lifetime excitations.

To see the changes in the dispersion due to the screening effect in more detail, the trace of peaks is extracted from both Fig. 8 and Fig. 9 and combined as depicted in Fig. 10. From Fig. 10 we can clearly notice the decay of an amplitude of the dispersion curves as a result of screening. The decay has nearly the same impact for both liquid [Figs. 10(a) and 10(b)] and solid [Figs. 10(c) and 10(d)] states. Therefore, screening results in a redshift of the collective excitation spectra. This shift in dispersion curves of $L(k, \omega)$ and $T(k, \omega)$ implies the changes in values of the respective sound speeds.
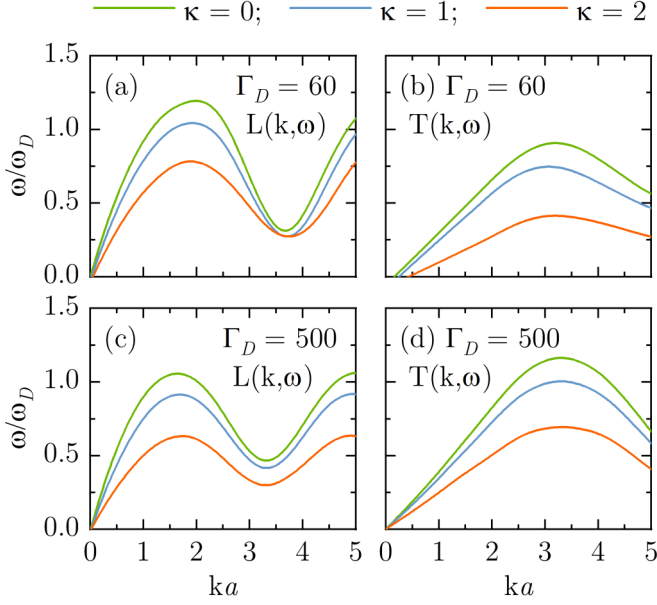
FIG. 10. The peaks of the dispersion relation (obtained from Figs. 3 and 4) at (a) and (b) liquid, and (c) and (d) solid states of 2D electric dipole systems. The green (upper), blue (mid), and orange (lower) curves correspond to $\kappa = 0$, 1, and 2, respectively.

Sound speeds were calculated in the long-wavelength regime ($k \to 0$) through the equation

$$\lim_{k \to 0} \frac{\omega}{k} = s_{L/T},$$

where s_L and s_T denote longitudinal and transverse sound speed, respectively.

The results of sound speed calculations for the solid state are summarized in Table III, from which we see that the longitudinal sound speed is decreased by 23% as $\kappa = 0$ is increased to $\kappa = 1$, and dropped by 50% at $\kappa = 2$ compared to the nonscreened case. For transverse sound speeds, we estimated a 9% drop at $\kappa = 1$ and a 33% drop at $\kappa = 2$.

In the liquid state, $\Gamma_D = 60$, longitudinal sound speeds are $s_L \approx 1.147 \, \omega_D a$ at $\kappa = 0$, $s_L \approx 0.881 \, \omega_D a$ at $\kappa = 1$, and $s_L \approx 0.594 \, \omega_D a$ at $\kappa = 2$. The changes of longitudinal sound speeds due to the screening in percentage ratio are about the same as in the solid state.

In the liquid state, we cannot find transverse sound speeds, because of a "q-gap," i.e., the domain at $ka \ll 1$ where transverse excitations are absent [52] [see Fig. 10(b)]. From Fig. 10(b) one can observe that screening results in a larger "q-gap." For example, the "q-gap" is increased from $ka \approx 0.17$ in the case of $\kappa = 0$ to $ka \approx 0.26$ at $\kappa = 1$, and then to $ka \approx 0.44$ at $\kappa = 2$.

TABLE III. Longitudinal s_L and transverse s_T sound speed values of 2D dipole systems at $\Gamma_D = 500$ and for three values of screening parameter κ.

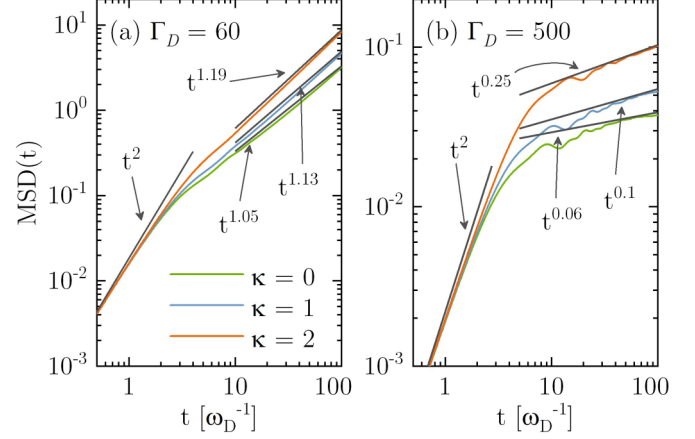| κ	0	1	2
$s_L/\omega_D a$	1.167	0.895	0.594
$s_T/\omega_D a$	0.378	0.343	0.252

FIG. 11. The mean-square displacement (MSD) of particles evaluated at (a) liquid ($\Gamma_D = 60$) and (b) solid ($\Gamma_D = 500$) states for three values of κ. Solid black lines are tangent to the MSD curves at time intervals $t\omega_D < 0.5$ and $50 < t\omega_D < 100$ with slopes corresponding to diffusion exponent γ in Eq. (19). The green (lower), blue (mid), and orange (upper) curves correspond to $\kappa = 0$, 1, and 2, respectively.

B. Mean-square displacement

Now, we turn our attention to the mean-square displacement (MSD) of particles, which is related to the diffusive characteristics of the system. In particular, we investigated the impact of screening on MSD. The MSD is calculated through the equation

$$\text{MSD}(t) = \langle |\mathbf{r}(t) - \mathbf{r}(0)|^2 \rangle.$$

The MSD can be used to classify the diffusion type in liquids by noting the proportionality

$$\text{MSD}(t) \propto t^\gamma, \tag{19}$$

where γ is the diffusion exponent, which defines the motion as follows: $\gamma = 2$, ballistic; $\gamma = 1$, diffusive; and $\gamma \neq 1$, anomalous.

The physically meaningful data on the MSD are limited with respect to time due to the finite length of a simulation box [53–55]. This limit is estimated as L/s_L. Using the above-calculated values of the sound speed, s_L, we estimated that for $N = 5041$ (with $L = \sqrt{\pi N} a$) the meaningful time intervals are $t^{\kappa=0} < 107 \, \omega_D^{-1}$, $t^{\kappa=1} < 140 \, \omega_D^{-1}$, and $t^{\kappa=2} < 211 \, \omega_D^{-1}$. Figure 11 presents the results of MSD calculations for 2D electric dipole systems at liquid ($\Gamma_D = 60$) and solid ($\Gamma_D = 500$) states with three different values of κ. Solid black lines in Fig. 11, which are shown tangent to each curve, serve to display the behavior of each MSD curve and classify the motion type in accordance with Eq. (19) at time intervals $t\omega_D < 0.5$ and $50 < t\omega_D < 100$.

In both liquid and solid states, the beginning of the particles' MSD is characterized by the ballistic motion. After about $t\omega_D \approx 2$ the effect of screening becomes evident, which is indicated by the shift of curves to larger values. These shifts imply that, at both $\Gamma_D = 60$ and 500, particles become more mobile with increasing κ.

If we consider two cases in more detail, first at $\Gamma_D = 60$, we note from Fig. 11(a) the increase of the diffusion exponent

from $\gamma \approx 1.05$ (almost normal diffusion) when there is no screening to $\gamma \approx 1.13$ at $\kappa = 1.0$, and to $\gamma \approx 1.19$ at $\kappa = 2.0$. This clearly shows the emergence of superdiffusive motion as a result of screening in the case of a liquid state at $50 < t\omega_D < 100$.

In the case of a solid state, at $\Gamma_D = 500$, the MSD curve of $\kappa = 0$ in Fig. 11(b) has a very low diffusion exponent $\gamma \approx 0.06$, which is explained by the fact that in a crystal most particles wander around a point, i.e., caged. The same behavior is observed in the studies of transport coefficients of classical 2D Yukawa systems when the coupling parameter is chosen large [53]. The diffusion exponent changes to $\gamma \approx 0.1$ at $\kappa = 1$ and noticeably to $\gamma \approx 0.25$ when we set $\kappa = 2$. Therefore, screening results in more mobile particles.

We note that the above-estimated diffusion exponents are valid only at $t\omega_D < 100$. Data presented for $t\omega_D \sim 100$ do not imply the limiting values of diffusion rates at long times. Note that the determination of such a limiting diffusion rate value for 2D strongly correlated liquids is still an open problem (see, e.g., Ref. [56]). The simulations of 2D Yukawa liquids indicated that the diffusion exponent has a trend toward unity at long time scales ($t > 10^5 \omega_p$, with ω_p being the plasma oscillation frequency) [54]. It is probable that the diffusion exponent of the 2D dipole system in the liquid state will show a similar behavior at sufficiently long times. The confirmation of this requires further research with a much larger number of particles and much longer times of simulation.

VI. CONCLUSIONS

We investigated the 2D system of electric dipoles in screening bulk media. The effect of screening on structural and dynamical properties and phase transition points was presented.

In the case of dynamical properties, the screening impact manifests in the decrease of dispersion relation amplitudes of both longitudinal and transverse waves. It was shown that the sound wave velocity decreases due to screening. Diffusive properties of 2D dipole systems also undergo changes as a result of screening. In the liquid state, the motion switches from normal to anomalous type (superdiffusion) at $50 < t\omega_D < 100$, and in the solid state the displacement of particles from a stationary point becomes more substantial.

The analysis of RDF data shows that the system loses its structural order due to screening, which is also indicated by the drop in the values of orientational and polygon order parameters. The fact that the structural order in the system diminishes as the degree of screening increases means that the solid-liquid transition of the system is forced to occur at larger values of the coupling parameter (lower temperatures).

The investigation of the behavior of the disorder parameter (which is based on the polygon construction method) in 2D dipole systems during melting and freezing points has been performed. A comprehensive analysis of the value of the disorder parameter corresponding to the melting as well as freezing points has been realized with the help of such quantities as the overall and local OOPs, and the potential energy of the system. As a result, it was revealed that the phase transition of the system occurs when the sum of nontriangular polygon order parameters (i.e., the disorder parameter) has a value 0.165. Moreover, we found that the local orientational order parameter [given by Eq. (15)] has a value 0.67 at the phase transition point. These results are valid for three different potentials [with $\kappa = 0$, 1, and 2 in Eq. (12)]. In analogy with previous studies of the universality of the orientational order parameter value for the phase transition [37], it is expected that the obtained values of the disorder and local orientational order parameters corresponding to the phase transition point are universal for other 2D systems with a repulsive pair potential.

We emphasize that the average orientational order parameter [computed using Eq. (14)] effectively captures the melting point, but not the freezing point during dynamic cooling (i.e., with a finite cooling rate). This was also observed in experiments [48]. Simulation results clearly show that the local orientational order parameter [see Eq. (15)] and the disorder parameter are more suitable for the investigation of freezing.

[1] M. Lemeshko, R. V. Krems, J. M. Doyle, and S. Kais, Manipulation of molecules with electromagnetic fields, Mol. Phys. **111**, 1648 (2013).

[2] S. A. Khrapak, N. P. Kryuchkov, and S. O. Yurchenko, Thermodynamics and dynamics of two-dimensional systems with dipolelike repulsive interactions, Phys. Rev. E **97**, 022616 (2018).

[3] G. I. Sukhinin and A. V. Fedoseev, Formation of a trapped-ion cloud around a dust particle in low-density plasma, IEEE Trans. Plasma Sci. **38**, 2345 (2010).

[4] G. Lapenta, Dipole Moments on Dust Particles Immersed in Anisotropic Plasmas, Phys. Rev. Lett. **75**, 4409 (1995).

[5] H. Schmidle, C. K. Hall, O. D. Velev, and S. H. L. Klapp, Phase diagram of two-dimensional systems of dipole-like colloids, Soft Matter **8**, 1521 (2012).

[6] A. Schella, A. Melzer, C. July, and C. Bechinger, Effect of confinement on the mode dynamics of dipole clusters, Soft Matter **11**, 1197 (2015).

[7] E. Janai, A. P. Cohen, A. V. Butenko, A. B. Schofield, M. Schultz, and E. Sloutskin, Dipolar colloids in apolar media: direct microscopy of two-dimensional suspensions, Sci. Rep. **6**, 28578 (2016).

[8] M. H. G. de Miranda, A. Chotia, B. Neyenhuis, D. Wang, G. Quéméner, S. Ospelkaus, J. L. Bohn, J. Ye, and D. S. Jin, Controlling the quantum stereodynamics of ultracold bimolecular reactions, Nat. Phys. **7**, 502 (2011).

[9] K. I. Golden, G. J. Kalman, P. Hartmann, and Z. Donkó, Dynamics of two-dimensional dipole systems, Phys. Rev. E **82**, 036402 (2010).

[10] K. I. Golden, G. J. Kalman, Z. Donko, and P. Hartmann, Acoustic dispersion in a two-dimensional dipole system, Phys. Rev. B **78**, 045304 (2008).

[11] S. De Palo, F. Rapisarda, and G. Senatore, Excitonic Condensation in a Symmetric Electron-Hole Bilayer, Phys. Rev. Lett. **88**, 206401 (2002).

[12] P. Ludwig, A. V. Filinov, M. Bonitz, and Yu. E. Lozovik, Ground state and structural transitions in mesoscopic electron-hole bilayers, Contrib. Plasma Phys. **43**, 285 (2003).

[13] P. Ludwig, A. Filinov, Yu. E. Lozovik, H. Stolz, and M. Bonitz, Crystallization in mass-asymmetric electron-hole bilayers, Contrib. Plasma Phys. **47**, 335 (2007).

[14] S. Ranganathan and R. E. Johnson, Diffusion and phase diagram of an electron-hole bilayer: A molecular dynamics study, Phys. Rev. B **75**, 155314 (2007).

[15] A. Tiene, J. Levinsen, M. M. Parish, A. H. MacDonald, J. Keeling, and F. M. Marchetti, Extremely imbalanced two-dimensional electron-hole-photon systems, Phys. Rev. Res. **2**, 023089 (2020).

[16] J. P. Hansen and I. R. McDonald, *Theory of Simple Liquids* (Academic, Oxford, 2013).

[17] N. H. March and M. P. Tosi, *Introduction to Liquid State* (World Scientific, Singapore, 2002).

[18] G. I. Sukhinin, A. V. Fedoseev, and M. V. Salnikov, Effect of ion mean free path length on plasma polarization behind a dust particle in an external electric field, Contrib. Plasma Phys. **59**, e201800152 (2019).

[19] G. Sukhinin, M. Salnikov, A. Fedoseev, and A. Rostom, Plasma polarization and wake formation behind a dust particle in an external electric field, IEEE Trans. Plasma Sci. **46**, 749 (2018).

[20] Zh. A. Moldabekov, P. Ludwig, J. P. Joost, and M. Bonitz, On the induced charge density distribution in streaming plasmas, Phys. Sci. Technol. **5**, 10 (2019).

[21] G. I. Sukhinin, A. V. Fedoseev, and M. V. Salnikov, Polarization of a dust particle and surrounded plasma in an external electric field, Contrib. Plasma Phys. **56**, 397 (2016).

[22] Y. Zhang, S. Li, W. Yan, Y. Qiang, and S. D. Tse, Role of dipole-dipole interaction on enhancing brownian coagulation of charge-neutral nanoparticles in the free molecular regime, J. Chem. Phys. **134**, 084501 (2011).

[23] R. Kompaneets, G. E. Morfill, and A. V. Ivlev, Wakes in complex plasmas: A self-consistent kinetic theory, Phys. Rev. E **93**, 063201 (2016).

[24] T. S. Ramazanov, Zh A. Moldabekov, and M. T. Gabdullin, Multipole expansion in plasmas: Effective interaction potentials between compound particles, Phys. Rev. E **93**, 053204 (2016).

[25] S. Sundar and Z. A. Moldabekov, Ultracold ions wakein dusty plasmas, New J. Phys. **22**, 033028 (2020).

[26] M. Mittal, P. P. Lele, E. W. Kaler, and E. M. Furst, Polarization and interactions of colloidal particles in ac electric fields, J. Chem. Phys. **129**, 064513 (2008).

[27] C. Alvarez and G. Tellez, Screening of charged spheroidal colloidal particles, J. Chem. Phys. **133**, 144908 (2010).

[28] S. van Teeffelen, H. Löwen, and C. N. Likos, Crystallization of magnetic dipolar monolayers: a density functional approach, J. Phys.: Condens. Matter **20**, 404217 (2008).

[29] S. Z. Lin, B. Zheng, and S. Trimper, Computer simulations of two-dimensional melting with dipole-dipole interactions, Phys. Rev. E **73**, 066106 (2006).

[30] H. Löwen, Dynamical criterion for two-dimensional freezing, Phys. Rev. E **53**, R29 (1996).

[31] T. Dornheim, J. Vorberger, S. Groth, N. Hoffmann, Zh. A. Moldabekov, and M. Bonitz, The static local field correction of the warm dense electron gas: An *ab initio* path integral monte carlo study and machine learning representation, J. Chem. Phys. **151**, 194104 (2019).

[32] L. A. Mistryukova, N. P. Kryuchkov, S. A. Khrapak, I. S. Golyak, and S. O. Yurchenko, Collective excitations in two-dimensional fluid with dipole-like repulsive interactions, J. Phys.: Conf. Ser. **1348**, 012097 (2019).

[33] B. I. Halperin and D. R. Nelson, Theory of Two-Dimensional Melting, Phys. Rev. Lett. **41**, 121 (1978).

[34] D. R. Nelson and B. I. Halperin, Dislocation-mediated melting in two dimensions, Phys. Rev. B **19**, 2457 (1979).

[35] K. J. Strandburg, Two-dimensional melting, Rev. Mod. Phys. **60**, 161 (1988).

[36] I. V. Schweigert, V. A. Schweigert, and F. M. Peeters, Melting of the Classical Bilayer Wigner Crystal: Influence of Lattice Symmetry, Phys. Rev. Lett. **82**, 5293 (1999).

[37] I. V. Schweigert, V. A. Schweigert, and F. M. Peeters, Enhanced stability of the square lattice of a classical bilayer Wigner crystal, Phys. Rev. B **60**, 14665 (1999).

[38] M. A. Glaser and N. A. Clark, Melting and liquid structure in two dimensions, Adv. Chem. Phys. **83**, 543 (1993).

[39] M. A. Glaser and N. A. Clark, Statistical geometry of simple liquids in two dimensions, Phys. Rev. A **41**, 4585 (1990).

[40] P. J. Steinbach and B. R. Brooks, New spherical-cutoff methods for long-range forces in macromolecular simulation, J. Comput. Chem. **15**, 667 (1994).

[41] L. Onsager, Electric moments of molecules in liquids, J. Am. Chem. Soc. **58**, 1486 (1936).

[42] V. Rokhlin, Rapid solution of integral equations of classical potential theory, J. Comput. Phys. **60**, 187 (1985).

[43] C. J. Fennell and J. Daniel Gezelter, Is the Ewald summation still necessary? Pairwise alternatives to the accepted standard for long-range electrostatics, J. Chem. Phys. **124**, 234104 (2006).

[44] M. Lamichhane, J. Daniel Gezelter, and K. E. Newman, Real space electrostatics for multipoles. I. Development of methods, J. Chem. Phys. **141**, 134109 (2014).

[45] D. Wolf, P. Keblinski, S. R. Phillpot, and J. Eggebrecht, Exact method for the simulation of Coulombic systems by spherically truncated, pairwise r^{-1} summation, J. Chem. Phys. **110**, 8254 (1999).

[46] M. Lamichhane, K. E. Newman, and J. Daniel Gezelter, Real space electrostatics for multipoles. II. Comparisons with the Ewald sum, J. Chem. Phys. **141**, 134110 (2014).

[47] P. Hartmann, G. J. Kalman, Z. Donkó, and K. Kutasi, Equilibrium properties and phase diagram of two-dimensional Yukawa systems, Phys. Rev. E **72**, 026409 (2005).

[48] Z. Wang, A. M. Alsayed, A. G. Yodh, and Y. Han, Two-dimensional freezing criteria for crystallizing colloidal monolayers, J. Chem. Phys. **132**, 154501 (2010).

[49] A. Radzvilavičius, Geometrical defects in two-dimensional melting of many-particle Yukawa systems, Phys. Rev. E **86**, 051111 (2012).

[50] W. D. Suranga Ruhunusiri, J. Goree, Y. Feng, and B. Liu, Polygon construction to investigate melting in two-dimensional

strongly coupled dusty plasma, Phys. Rev. E **83**, 066402 (2011).

[51] J. P. Hansen, I. R. McDonald, and E. L. Pollock, Statistical mechanics of dense ionized matter. III. Dynamical properties of the classical one-component plasma, Phys. Rev. A **11**, 1025 (1975).

[52] N. P. Kryuchkov, L. A. Mistryukova, V. V. Brazhkin, and S. O. Yurchenko, Excitation spectra in fluids: How to analyze them properly, Sci. Rep. **9**, 10483 (2019).

[53] Z. Donko, J. Goree, P. Hartmann, and B. Liu, Time-correlation functions and transport coefficients of two-dimensional Yukawa liquids, Phys. Rev. E **79**, 026401 (2009).

[54] T. Ott and M. Bonitz, Is Diffusion Anomalous in Two-Dimensional Yukawa Liquids? Phys. Rev. Lett. **103**, 195001 (2009).

[55] Y. Q. Aldakulov, Zh. A. Moldabekov, M. Muratov, and T. S. Ramazanov, Subdiffusion of dust particles in cryogenic plasmas, Jpn. J. Appl. Phys. **59**, SHHE02 (2020).

[56] P. Hartmann, J. C. Reyes, E. G. Kostadinova, L. S. Matthews, T. W. Hyde, R. U. Masheyeva, K. N. Dzhumagulova, T. S. Ramazanov, T. Ott, H. Kählert, M. Bonitz, I. Korolov, and Z. Donkó, Self-diffusion in two-dimensional quasimagnetized rotating dusty plasmas, Phys. Rev. E **99**, 013203 (2019).